

Particle Levitation Velocimetry for boundary layer measurements in high Reynolds number liquid helium turbulence

Yinghe Qi^{1,2} and Wei Guo^{1,2,*}

¹National High Magnetic Field Laboratory, 1800 East Paul Dirac Drive, Tallahassee, Florida 32310, USA

²Mechanical Engineering Department, FAMU-FSU College of Engineering, Tallahassee, Florida 32310, USA

*wguo@magnet.fsu.edu

ABSTRACT

Understanding boundary layer flows in high Reynolds number (Re) turbulence is crucial for advancing fluid dynamics in a wide range of applications, from improving aerodynamic efficiency in aviation to optimizing energy systems in industrial processes. However, generating such flows requires complex, power-intensive large-scale facilities. Furthermore, the use of local probes, such as hot wires and pressure sensors, often introduces disturbances due to the necessary support structures, compromising measurement accuracy. In this paper, we present a solution that leverages the vanishingly small viscosity of liquid helium to produce high Re flows, combined with an innovative Particle Levitation Velocimetry (PLV) system for precise flow-field measurements. This PLV system uses magnetically levitated superconducting micro-particles to measure the near-wall velocity field in liquid helium. Through comprehensive theoretical analysis, we demonstrate that the PLV system enables quantitative measurements of the velocity boundary layer over a wall unit range of $44 \leq y^+ \leq 4400$, with a spatial resolution that, depending on the particle size, can reach down to about $10 \mu\text{m}$. This development opens new avenues for exploring turbulence structures and correlations within the thin boundary layer that would be otherwise difficult to achieve.

Introduction

Turbulent boundary layer flows are fundamental to numerous engineering applications. For instance, dissipation in these flows controls aerodynamic forces and heating in hypersonic vehicles and accounts for over 50% of surface drag in aircraft, as well as nearly 95% of energy loss in long-distance pipeline transport^{1,2}. Many of these applications involve flows at very high Reynolds numbers (Re), where the turbulent boundary layer is characterized by near-wall small-scale structures, such as streaks and vortices, as well as larger, energetic eddies in the outer region^{3,4}. The interaction between these scales at high Re intensifies turbulence and increases the complexity of flow dynamics. To better understand these interactions, it is crucial to precisely quantify turbulence characteristics within the boundary layer, including the scaling behaviors of mean velocity and turbulence intensity. This knowledge is vital for developing more accurate and predictive turbulence models, which are essential for optimizing designs and enhancing performance in practical engineering applications.

The mean velocity profile $\overline{U}_x(y)$ in the streamwise direction near a solid wall in fully developed turbulent flows has been studied extensively and is known to consist of three distinct regions along the coordinate y perpendicular to the wall³⁻⁵. The inner region, dominated by viscous effects, typically extends from the wall to $y^+ = y/y^* = 50$, where $y^* = \nu/u_\tau$ denotes the viscous length scale⁶. In this expression, ν is the kinetic viscosity, and $u_\tau = (\tau_w/\rho_f)^{1/2}$ is the viscous velocity, with τ_w being the wall shear stress and ρ_f the fluid density. At sufficiently large y , for example beyond $y/R \approx 0.12$ in pipe flows with a pipe radius R , the wake region emerges, where $\overline{U}_x(y)$ depends on overall flow conditions. Between these two regions lies the overlap region, where $\overline{U}_x(y)$ follows a universal logarithmic profile, commonly referred to as the “law of the wall” or “log law”, expressed as $U^+ = \frac{1}{\kappa} \ln y^+ + B$ ³⁻⁵. Here, $U^+ = \overline{U}_x/u_\tau$, and κ and B are the von Kármán constant and the additive constant, respectively. Despite extensive experimental⁷⁻¹² and numerical¹³⁻¹⁵ investigations, some key issues remain unsolved, such as the extent and Re dependence of the log law and the precise values of these constants^{16,17}. The Princeton Superpipe experiments suggest that the log law appears in the range $600 \leq y^+ \leq 0.12R/y^*$ when the pipe Reynolds number exceeds about 2.3×10^5 ^{3,7,18,19}. These experiments reported a von Kármán constant $\kappa = 0.42$, which differs from the typical values of 0.37–0.39 observed in high-Re boundary layer and channel flows^{10,12,20-22}, raising questions about the universality of κ across different flow types. However, more recent high-Re pipe flow data from Furuichi *et al.*, using the “Hi-Reff” facility in Japan, suggest a κ value of 0.385, indicating a potential degree of universality for κ ^{8,23}. Given the pivotal role of κ in modeling and numerical simulations of wall-bounded flows, further independent high-Re flow measurements are necessary.

In high-Re turbulence experiments, velocity field measurements have predominantly relied on hot-wire anemometers and

pressure sensors^{24–26}. These sensors normally have relatively large sizes, limiting their spatial resolution and effectiveness in capturing the fine details of boundary layer flows. For instance, conventional hot-wire sensors are difficult to reduce below 0.25 mm in length. In response, efforts have been made to miniaturize these sensors. As an example, Smits’ team developed hot-wire sensors with an active length as small as 30 μm ^{7,27}. Similarly, advances have also been made in pressure sensor technology²⁸. However, despite these miniaturization efforts, both types of sensors still face one challenging issue: they require support structures attached to the wall, which inevitably introduce flow disturbances. These disturbances compromise the collection of clean data in high-Re turbulent flows, particularly in thin boundary layers, where minimizing interference is crucial for accurate measurements. In addition to hot-wire anemometry and pressure sensors, non-intrusive measurement techniques based on direct flow visualization have been widely applied to measure velocity fields in various types of flows. Particle Image Velocimetry (PIV) and Particle Tracking Velocimetry (PTV) are two commonly used flow visualization methods^{29–38}. However, both methods face limitations in spatial resolution when applied to velocity field measurements in high-Re turbulent boundary layers, restricting their ability to resolve thin boundary layer structures^{39,40}. Another non-intrusive technique is Molecular Tagging Velocimetry (MTV), which has been applied in various flow conditions, including studies of wall shear stress and velocity profiles^{41–47}. However, typical MTV setups can only capture the velocity component perpendicular to the tracer lines, and their spatial resolution is constrained by the displacement of the tracer lines, typically on the order of $10^2 \mu\text{m}$ ⁴⁸. This limitation reduces its effectiveness for capturing fine-scale boundary layer structures in high-Re turbulence.

To overcome these limitations, we propose an approach that combines liquid helium (LHe) as the working fluid with a novel measurement technique called Particle Levitation Velocimetry (PLV), which utilizes magnetically levitated superconducting micro-particles as probes. LHe’s exceptionally low kinematic viscosity, i.e., nearly three orders of magnitude lower than that of ambient air⁴⁹, allows for the generation of very high-Re flows in compact facilities^{50–52}, which is difficult to achieve with conventional fluids. Moreover, LHe provides a cryogenic environment suitable for superconducting coils and particles, enabling magnetic levitation of micro-particle probes in LHe without physical supports to disturb the flow.

In this paper, we present the design and analysis of the PLV system, integrated with our Liquid Helium Flow Visualization Facility (LHFVF), which can generate turbulent pipe flows with Re exceeding 10^{653} . The PLV system uses a compact four-coil setup to create a three-dimensional trap with adjustable size and streamwise gradient, enabling easy particle loading while stably levitating superconducting micro-particles near the pipe wall, preventing them from being swept away by high-Re flows. Comprehensive simulations were conducted to calculate the potential energy of the particles in the magnetic trap and to model their motion under both static and high-Re flow conditions. The results show that when the flow is initiated, the particles move downstream due to the fluid’s drag force, undergoing damped oscillations before settling into a new equilibrium position. By measuring the particle’s mean displacement, we can determine the drag force and consequently calculate the mean flow velocity at the corresponding levitation height. Furthermore, by introducing random velocity fluctuations into the simulations, we established the correlation between particle position fluctuations and velocity fluctuations in the flow, enabling the evaluation of near-wall velocity fluctuations. The levitation height can be adjusted continuously by tuning the coil currents. Our simulations indicate that the PLV system can measure the velocity field across a wide range of wall units $44 \leq y^+ \leq 4400$. By implementing multiple levitated particles, this system may provide new opportunities to study turbulence structures and correlations in the boundary layer that would be otherwise difficult to achieve.

Results

Liquid Helium Flow Facility and Particle Levitation

As shown schematically in Figure 1a, the LHFVF is a cryostat designed for generating and visualizing LHe pipe flows. This facility includes a 5-meter-long horizontal cylindrical chamber with an inner diameter of 0.2 m, housed inside the evacuated cryostat body and enclosed by two concentric radiation shields that are cooled by natural circulation loops connected to the liquid helium and nitrogen tanks. A 3.35-meter-long pipe with a square cross-section ($2 \times 2 \text{ cm}^2$) is positioned at the chamber center, connected to helium storage stacks at both ends, where the LHe temperature is controlled by regulating the vapor pressure. The system is equipped with three sets of windows: two vertical sets to allow laser beams to pass through the top and bottom of the pipe, and a side window set for capturing flow images using a high-speed camera. Each set consists of three windows mounted on the vacuum and the two radiation shields. To drive the LHe flow, a bellows pump is installed in the left helium storage stack. This bellows pump, with a cross-sectional area of $1.8 \times 10^{-2} \text{ m}^2$ and a stroke length of 9.4 cm, can displace up to 1.7 liters of LHe. The bellows is connected to a linear actuator, driven by a computer-controlled stepper motor, capable of producing enough thrust to drive the LHe through the pipe at pipe Reynolds numbers exceeding 10^{653} .

To probe the flow, we propose to adopt the PLV system, which consists of superconducting niobium particles, i.e., microspheres with diameters $d_p = 10 - 50 \mu\text{m}$, and a superconducting coil system for levitating them. Below its critical temperature $T_c = 9.2 \text{ K}$, niobium becomes superconducting. At LHe temperature of 4.2 K, the lower critical field of niobium is about 0.15 T⁵⁴. Below this field strength, the niobium particles exhibit perfect diamagnetism, with a volume magnetic susceptibility χ close to -1 as compared to typical values of -10^{-5} to -10^{-6} for ordinary diamagnetic materials^{55,56}. This makes them much

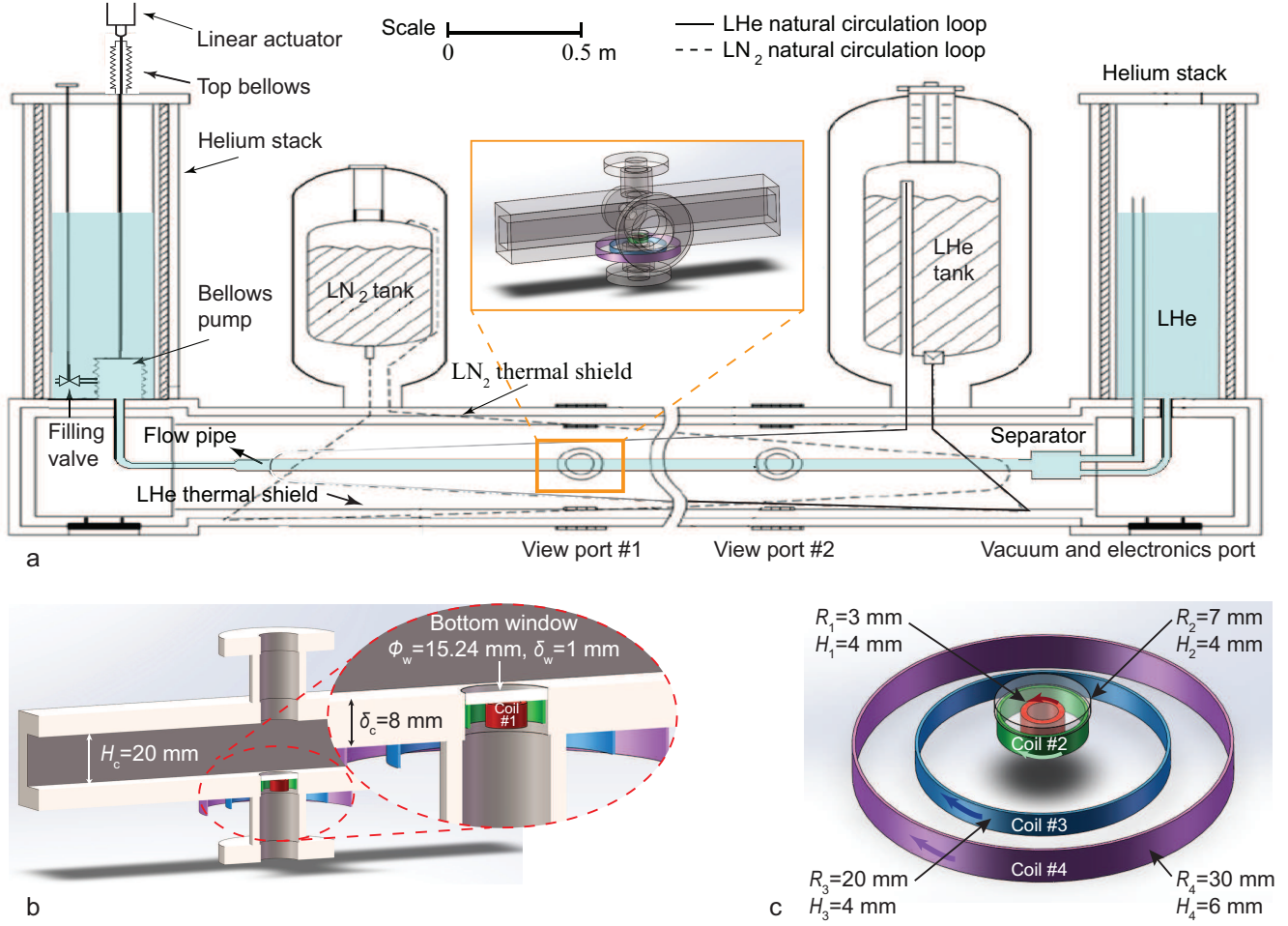


Figure 1. Pipe flow and particle levitation facility. **a** Schematic diagram of the Liquid Helium Flow Visualization Facility. **b** A schematic showing the locations of the coils for particle levitation. **c** A schematic showing the coil specifications.

easier to levitate using relatively weak magnetic fields. Additionally, niobium is easier to fabricate and machine than many other superconducting materials, making it a practical choice for used in the PLV system.

When a superconducting niobium particle is placed in a magnetic field $\mathbf{B}(\mathbf{r})$, it experiences a potential energy per unit volume given by⁵⁷:

$$E(\mathbf{r}) = (\rho_p - \rho_f) gy + \frac{1}{4} \frac{\mathbf{B}^2(\mathbf{r})}{\mu_0} \quad (1)$$

where $\rho_p = 8570 \text{ kg/m}^3$ and $\rho_f = 145 \text{ kg/m}^3$ are the densities of niobium and LHe, respectively, g represents gravitational acceleration, and μ_0 is the vacuum permeability. Levitation of the niobium particle can be achieved at a location where $\partial E(\mathbf{r})/\partial z = 0$. For stable levitation, $E(\mathbf{r})$ must increase in all directions from the levitation location.

Given the LHe environment, we choose to use superconducting coils to generate the magnetic field to avoid Joule heating. There are various design constraints to consider: the coils must fit around the window flange of the flow pipe, and the current in the coil wires must remain below the critical current to maintain the superconducting state. At the same time, the coils must provide a strong magnetic field gradient in both the vertical and the flow directions to levitate the niobium particles and to prevent the particles from being swept away by LHe in high Re flows. After thoroughly evaluating various coil configurations and current settings, we finally arrived at the optimal coil design, as illustrated schematically in Figure 1b and 1c.

This coil system consists of four concentric coils, coaxially aligned with the bottom window. Coils #1 and #2 are installed inside the window flange just below the 1-mm-thick bottom window, while Coils #3 and #4 are placed outside the window flange beneath the flow pipe. The radii of Coils #1, #2, #3, and #4 are 3 mm, 7 mm, 20 mm, and 30 mm, respectively. Each coil is constructed using copper-niobium titanium wires from SUPERCON Inc, capable of carrying up to $I_c = 6.8 \text{ A}$ at 4.2 K ⁵⁸. Coils #1, #2, and #3 each consist of 15 layers with 40 turns per layer, yielding a total of $N_1 = N_2 = N_3 = 600$ turns per coil.

With a wire thickness of $102\ \mu\text{m}$, 40 turns in each layer results in a coil height of 4 mm. Coils #4 also has 15 layers but 60 turns per layer, rendering a total of $N_4 = 900$ turns and a coil height of 6 mm. As we will present in subsequent sections, when suitable currents are applied to these coils, a three-dimensional potential trap can form where $E(\mathbf{r})$ exhibits a local minimum at the levitation location. As indicated in Figure 1c, the current in coil #1 flows in opposite direction to that in coils #2, #3, and #4. This configuration lowers the potential energy at the trap center while raising it along the sides, creating pancake-shaped trap elongated in the horizontal direction. This design facilitates easy particle loading and allows for convenient particle displacement control within the trap region, accommodating a wide range of LHe flow speeds.

Particle loading and levitation

Particle loading

The niobium particles need to be placed inside the flow pipe before the cryostat is cooled down. During the cooling process, the pipe will be pumped and flushed with helium gas. When LHe starts filling, the liquid may slosh in the pipe. The magnetic trap can be turned on only after the pipe is fully filled with LHe and the temperature drops below the superconducting transition temperature of the coils. Without the magnetic trap active, the flowing gaseous and liquid helium may carry the particles away from the window region, preventing their levitation in later measurements. To avoid this, a small pit (diameter: 0.5 mm; depth: 0.25 mm) can be carved into the bottom window to securely contain the particles. The pit is located at 2.25 mm downstream from the center of the bottom window. As will be discussed later, the maximum streamwise displacement of the particles in all the considered LHe flows is less than 2 mm from the trap center. Therefore, the pit would not affect the particles during the boundary layer measurements.

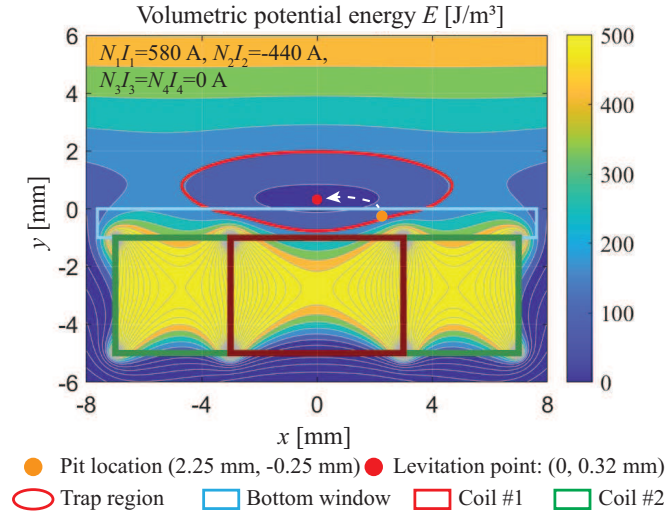


Figure 2. Contour plot of the volumetric potential energy for particle loading. Only Coils #1 and #2 are activated.

After the pipe is filled with LHe and cooled, we can transfer the niobium particles from the downstream pit to the center of the magnetic trap. To accomplish this, we activate only Coils #1 and #2 by applying currents of $I_1 = 0.97\ \text{A}$ and $I_2 = -0.73\ \text{A}$, yielding $N_1I_1 = 580\ \text{A}$ and $N_2I_2 = -440\ \text{A}$. These currents are well below the critical current I_c of the wire. The method for calculating the magnetic field $\mathbf{B}(\mathbf{r})$ generated by the coils is described in the Method section. Using the computed $\mathbf{B}(\mathbf{r})$, we can produce a contour plot of the volumetric potential energy $E(\mathbf{r})$, as shown in Figure 2. Given the concentric coil arrangement, $E(\mathbf{r})$ exhibits axial symmetry around the coil center axis. Figure 2 provides a cross-section view in the $x-y$ plane, where x is the axis in the flow direction, and the coordinate origin is set at the center of the bottom window surface. As depicted, a region with closed contours of $E(\mathbf{r})$ is formed, where $E(\mathbf{r})$ decreases towards the region center. This is the trapping region, where a niobium particle always experiences a net force directing it towards the center, allowing it to be stably levitated. For clarity, the boundary of the trapping region is marked in red. When only Coils #1 and #2 are activated with the specified currents, the radial confinement is relatively weak, and the trapping region extends to a large radius, covering the pit used for niobium particle storage. In this case, a niobium particle initially placed in the pit (the orange dot in Figure 2) will experience a net lifting force that transports it to the trap center located at $(x_0 = 0, y_0 = 0.32\ \text{mm})$, marked by the red dot.

Particle levitation and position control

After the niobium particle is loaded into the center of the magnetic trap, we can activate all four coils to create a more compact trapping region, suitable for flow field measurements in high-Re LHe flows. Figure 3a shows a representative contour plot

of $E(\mathbf{r})$ with currents $I_1 = 4.00$ A, $I_2 = -2.52$ A, $I_3 = -3.67$ A, $I_4 = -2.89$ A, yielding $N_1I_1 = 2400$ A, $N_2I_2 = -1510$ A, $N_3I_3 = -2200$ A, $N_4I_4 = -2600$ A. To provide a clearer view of the $E(\mathbf{r})$ profile around the levitation point, Figure 3 only shows the region near the bottom window and omits the visual representation of coils #3 and #4, although their contribution to $E(\mathbf{r})$ is fully accounted for in the calculations. In this configuration, the particle is levitated at $y_0 = 0.30$ mm. Compared to Figure 2 where only Coils #1 and #2 are activated, the addition of Coils #3 and #4 increases $E(\mathbf{r})$ at larger $|x|$ values. This results in a much more compact trapping region with steeper horizontal gradients. As we will discuss in the next section, the viscous drag force on the niobium particle from flowing LHe scales with d_p^2 , while the magnetic restoring force, being a body force, scales with d_p^3 . When the particle size is small and the LHe flow speed is high, a significant streamwise displacement of the particle can occur. The strong horizontal gradient of $E(\mathbf{r})$, achieved by activating all four coils, is crucial for confining the particle within the trap region in high-Re LHe flows. The four coil configuration also provides precise control over the height of the levitation point. For instance, Figure 3b shows the contour plot of $E(\mathbf{r})$ with the current in Coil #1 remaining the same as in Figure 3a and the currents in Coils #2, #3 and #4 decrease to $N_2I_2 = -900$ A, $N_3I_3 = -1500$ A and $N_4I_4 = -2400$ A, respectively. In this case, the height of the levitation point shifts to $y_0 = 0.98$ mm. Our numerical study suggests that the four-coil system enables precise adjustment of the particle levitation height from $y_0 = 20$ μm to $y_0 = 2$ mm for particles with diameters of $d_p = 15 - 50$ μm . In all the studied cases, the maximum magnetic field strength at the levitation point is 0.014 T, which is far below the lower critical field of niobium.

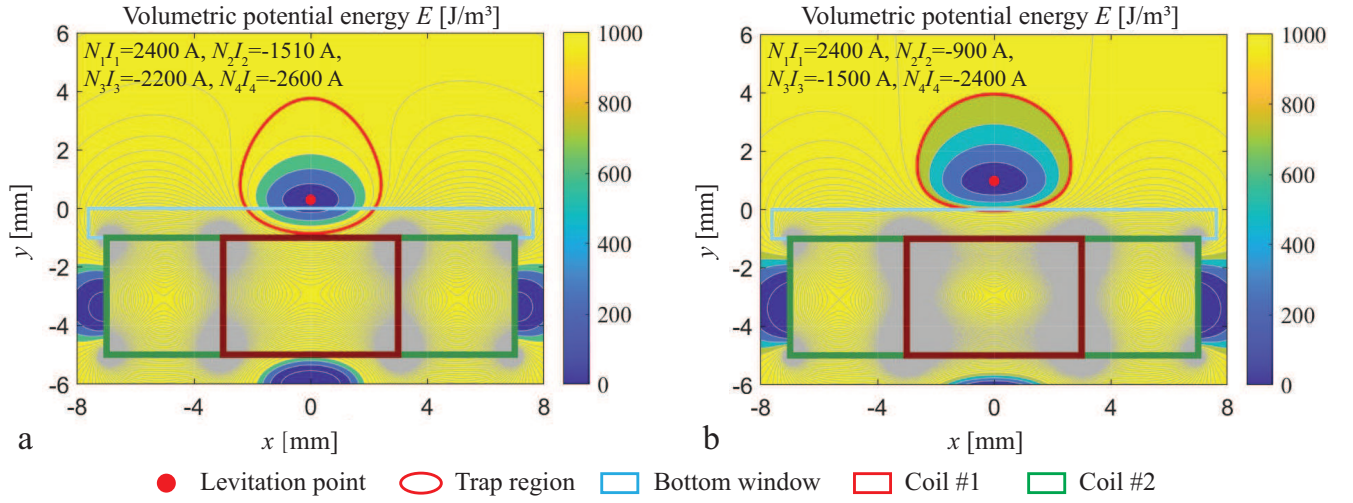


Figure 3. Contour plots of representative volumetric potential energy fields for particle levitation. a Configuration with the particle levitated at $y_0 = 0.30$ mm. **b** Configuration with the particle levitated at $y_0 = 0.98$ mm

Boundary layer study using PLV

Study of mean velocity

To illustrate how the PLV system can be utilized for measuring mean velocity profiles in the boundary layer, we begin by considering the equation of motion for the niobium particle, given by:

$$\rho_p V_p \frac{d^2 \mathbf{r}_p}{dt^2} = [-\nabla E(\mathbf{r})] V_p + \mathbf{F}_d \quad (2)$$

where \mathbf{r}_p is the position vector of the particle, $V_p = \frac{\pi}{6} d_p^3$ is the particle's volume, $-\nabla E(\mathbf{r})$ represents the volumetric force acting on the particle due to the combined effects of the magnetic field and gravity. The term \mathbf{F}_d represents the drag force exerted by the LHe flow within the pipe. Assuming the flow velocity of LHe at the particle's location is \mathbf{U}_f , the drag force \mathbf{F}_d is given by $\mathbf{F}_d = -\frac{3}{4} \frac{C_D \text{Re}_p \mu}{d_p} \mathbf{V}$ ⁵⁹, where $\mathbf{V} = \frac{d\mathbf{r}_p}{dt} - \mathbf{U}_f$ is the relative velocity between the particle and the LHe flow. The drag coefficient C_D can be calculated as⁵:

$$C_D \approx \frac{24}{\text{Re}_p} + \frac{6}{1 + \sqrt{\text{Re}_p}} + 0.4 \quad (3)$$

In this expression, $\text{Re}_p = \rho_f \mathbf{V} d_p / \mu$ is the particle Reynolds number, where μ is the dynamic viscosity of LHe. Eq. (3) applies for Re_p values in the range of $0 \leq \text{Re}_p \leq 2 \times 10^5$, which is valid for all the flows considered here.

Assuming a niobium particle initially held stationary at the center of the magnetic trap, Eq. (2) allows us to simulate its motion when a LHe flow is turned on at $t = 0$. As an example, Figure 4 shows the time evolution of the coordinates $x_p(t)$ and $y_p(t)$ for a particle with a diameter of $d_p = 50 \mu\text{m}$, initially levitated at $x_p(0) = x_0 = 0$ and $y_p(0) = y_0 = 0.98 \text{ mm}$. This simulation is based on a local flow velocity of $U_f = 0.47 \text{ m/s}$ in the x direction. Due to the drag force, the particle drifts downstream and exhibits a damped oscillation around the new equilibrium location at $x_{eq} = 1.04 \text{ mm}$. The drift in the y direction is negligible, and the oscillations are significantly weaker in this direction. To characterize the damping, we introduce a damping time scale τ_0 , defined as the time it takes for the particle's streamwise velocity to fall below 10^{-4} m/s . By this time, all the oscillations around the new equilibrium location are considered negligible. For the case shown in Figure 4a, τ_0 is about 0.13 s, which is much shorter than the time scale of about 10 s during which a steady flow can be maintained in the pipe by the bellows pump in a single stroke⁶⁰. The downstream displacement of the particle strongly depends on the flow velocity. Figure 4b shows the evolution of the streamwise coordinate $x_p(t)$ for the same particle as in Figure 4a but at three different flow velocity U_f . As U_f increases from 0.27 m/s to 0.47 m/s, the equilibrium displacement increases from about 0.4 mm to 1.04 mm. The correlation between x_{eq} and U_f obtained over the flow velocity U_f range from 0.1 to 0.47 m/s is shown in Figure 4c. This correlation can be well described by a second-order polynomial expression, $x_{eq} = aU_f^2 + bU_f + c$, with the coefficients a , b , and c provided in the figure. Therefore, by measuring the downstream displacement x_{eq} , one can use this correlation to determine the corresponding flow velocity U_f , a key concept of PLV. The coefficients a , b , and c depend on the particle size d_p and the initial levitation height y_0 , but they can be easily determined through the same analysis for different configurations.

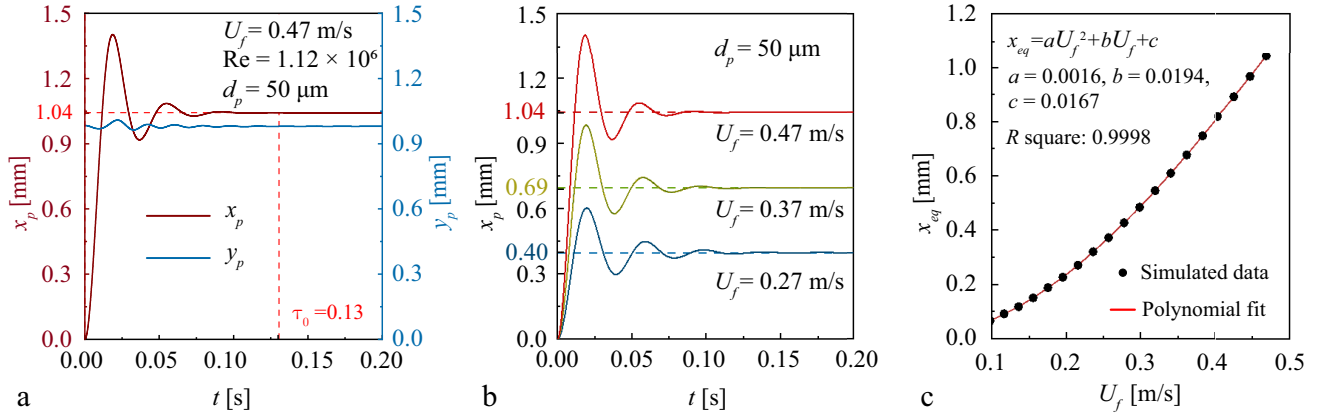


Figure 4. Position evolution of levitated particles in LHe flows. **a** Coordinate evolution for a particle with $d_p = 50 \mu\text{m}$, initially levitated at $y_0 = 0.98 \text{ mm}$, with a local LHe flow velocity of $U_f = 0.47 \text{ m/s}$. **b** Coordinate evolution of the same particle under different flow velocities. **c** Correlation between equilibrium position x_{eq} and local flow velocity U_f

To apply PLV for boundary layer velocity measurements, we can adjust the levitation height y_0 of the niobium particle. The local mean flow velocity varies at different heights, which results in the particle drifting different distances downstream. To illustrate this effect, consider a boundary layer described by the log law^{18,19}:

$$U^+ = \begin{cases} 8.7y^{+0.137}, & 50 < y^+ < 600 \\ \frac{1}{0.42} \ln(y^+) + 5.6, & 600 \leq y^+ \leq 0.12Ru_\tau/\nu. \end{cases} \quad (4)$$

For a particle levitated at $y_p = y_0$ from the pipe bottom surface, the corresponding wall unit is $y^+ = y_p u_\tau / \nu$, where the viscous velocity u_τ in He II pipe flows can be evaluated as $u_\tau = (\tau_w / \rho_f)^{1/2} = (\frac{1}{8} f U_{avg}^2)^{1/2}$, with U_{avg} being the mean velocity averaged over the pipe cross-section, and f being the measured friction factor for LHe pipe flows^{61,62}. Knowing the value of y^+ , the dimensionless mean velocity $U^+(y^+)$ can be determined from the above log-law expression. The mean streamwise velocity at height y_p in physical space is then given by $\bar{U}_f(y) = u_\tau U^+(y^+)$. Figure 5a shows the evolution of the $x_p(t)$ coordinate for particles with diameters $d_p = 15 - 50 \mu\text{m}$, levitated at different heights y_p from the bottom window surface in a LHe flow with $U_{avg} = 0.5 \text{ m/s}$, corresponding to a pipe Reynolds number of $Re = 1.12 \times 10^6$. The results clearly show that particles of a given size drift different distances depending on their location relative to the wall, resulting in different x_{eq} .

In a real PLV experiment, the process works in reverse. First, a particle is levitated at height y_0 , and then the flow is initiated. Once the particle settles at its equilibrium position, the downstream displacement x_{eq} is measured. Using the previously established correlation, the mean streamwise velocity, $\bar{U}_f(y_0)$, can be determined. By varying y_0 and repeating the

measurements, a near-wall mean velocity profile can be constructed. Nonetheless, when a particle is placed too close to the wall, the streamwise flow velocity \bar{U}_f becomes too low, resulting in a downstream displacement comparable to the particle's diameter d_p , making it difficult to resolve. Conversely, if the particle is placed too far from the wall, where the flow velocity is much higher, the displacement may exceed the boundaries of the magnetic trap, causing the particle to lose confinement. Since the viscous drag force on the particle F_d scales with d_p^2 , while the magnetic restoring force $[-\nabla E(\mathbf{r})]V_p$ scales with the particle volume V_p (and therefore d_p^3), smaller particles tend to drift farther downstream compared to larger particles at a given flow velocity. Therefore, small particles are more suitable for probing the velocity profile near the wall, where the velocity is low. On the other hand, larger particles are better suited for exploring regions farther from the wall, where the velocity is higher and the magnetic trap is less effective at confining smaller particles. In Figure 5b, we present the calculated range of the wall unit y^+ that can be explored by niobium particles of four different diameters, i.e., $d_p = 15, 20, 30,$ and $50 \mu\text{m}$, under the same LHe flow conditions shown in Figure 5a. By combining measurements using these different particles, we can explore the mean streamwise velocity $\bar{U}_f(y)$ over a wall unit range of $44 \leq y^+ \leq 4400$, covering the entire logarithmic law region and beyond, as illustrated in Figure 5b.

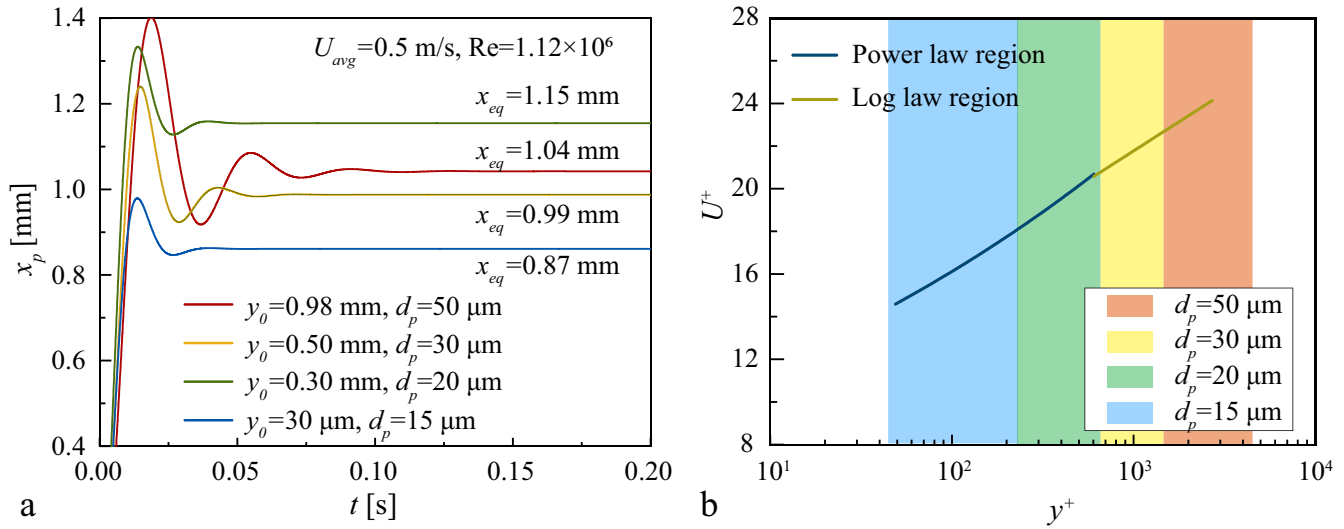


Figure 5. Boundary-layer mean velocity analysis. a Coordinate evolution of particles with different diameters d_p and levitated at varying heights y_0 under LHe flow with a pipe-averaged velocity of $U_{avg} = 0.5 \text{ m/s}$. b Range of wall units y^+ and the corresponding range of the dimensionless velocity U^+ that can be explored by these particles.

Study of turbulence intensity

After the particle settles at its new downstream equilibrium position, x_{eq} , in the presence of a LHe flow, turbulent eddies can cause it to fluctuate around this position. The amplitude of these fluctuations is expected to correlate with the velocity fluctuations, ΔU_f , in the LHe. By measuring the particle's position fluctuations, one can infer ΔU_f , providing insights into the turbulence intensity profile, $\Delta U_f(y)/\bar{U}_f(y)$, within the boundary layer. To demonstrate this, we conducted simulations by introducing random velocity fluctuations, $\Delta U_f(y)$, into the mean streamwise velocity, $\bar{U}_f(y)$, in the equation of motion for the niobium particle (i.e., Eq. (2)). Near the solid wall, turbulence is anisotropic, with streamwise velocity fluctuations dominating the other two directions⁴. In our simulation, we adopted streamwise velocity fluctuations, $\Delta U_f(y)$, based on the near-wall turbulence intensity profile reported by M. Hultmark, *et al.*⁷. For instance, for a niobium particle levitated at $y_0 = 30 \mu\text{m}$ from the bottom window surface in the presence of a LHe flow with a pipe averaged velocity of $U_{avg} = 0.5 \text{ m/s}$, the streamwise velocity fluctuation ΔU_f is 0.05 m/s . Figure 6a shows the time evolution of the x -coordinate for a particle with diameter $d_p = 15 \mu\text{m}$ in such a flow. In this simulation, we varied the flow velocity as $U_f(t) = \bar{U}_f + \Delta U_f(t)$ at each time step $\Delta t = 50 \mu\text{s}$, where ΔU_f follows a normal distribution with a root mean square value $\langle \Delta U_f^2(t) \rangle^{1/2} = 0.05 \text{ m/s}$. As seen in Figure 6a, the particle's x -coordinate fluctuates around the equilibrium location $x_{eq} = 0.87 \text{ mm}$. By analyzing the fluctuations in the time window from 0.1 s to 20 s , we obtain the mean fluctuation amplitude to be $\Delta x = \langle (x - x_{eq})^2 \rangle^{1/2} = 15.5 \mu\text{m}$. For practical PLV application, a correlation between Δx and ΔU_f is needed. To obtain this correlation, we repeated the simulation by varying ΔU_f in the range of 0.02 m/s to 0.065 m/s . The results are shown in Figure 6b, which reveal a strong linear correlation between Δx and ΔU_f as $\Delta x = a\Delta U_f$, with the coefficient a provided in the figure. Again, the coefficient a depends on the particle size d_p and the initial levitation height y_0 . For particles with different sizes and levitation heights, the correlation

between Δx and ΔU_f can be determined through similar numerical analysis. By experimentally measuring the fluctuations in particle motion at various levitation heights and applying the corresponding correlation tailored to each height, one can gain a comprehensive understanding of the turbulence intensity profile within the boundary layer.

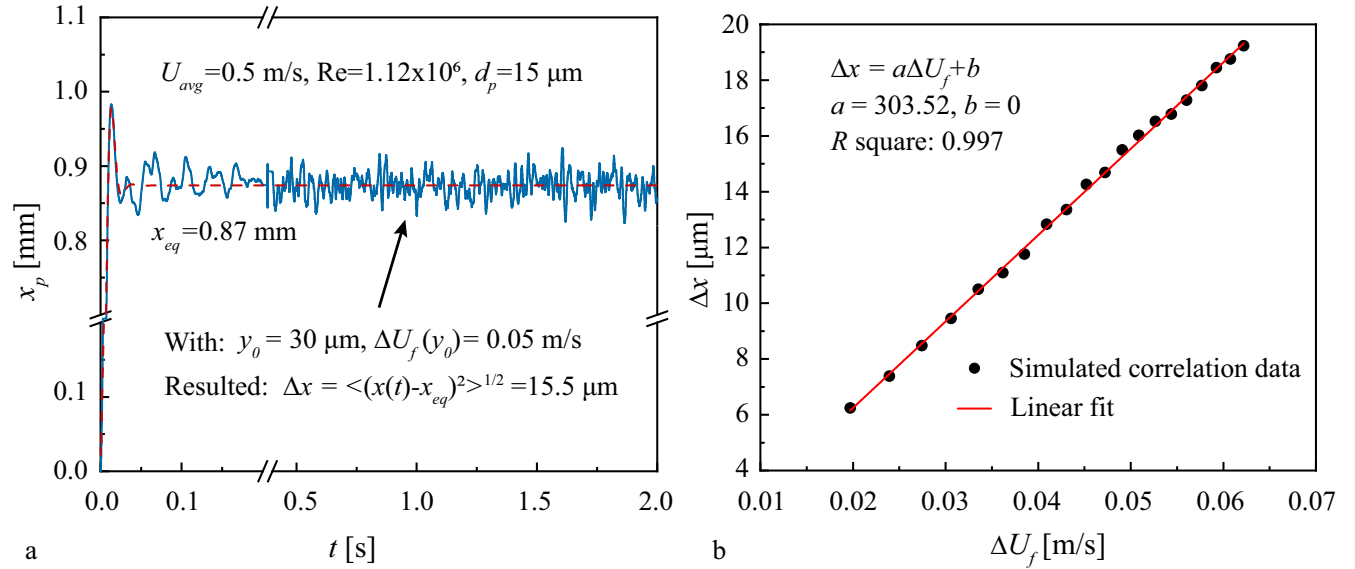


Figure 6. Boundary-layer velocity fluctuation analysis. **a** Coordinate evolution of a particle with $d_p = 15 \mu\text{m}$ levitated at $y_0 = 30 \mu\text{m}$ when a random velocity fluctuation with amplitude $\Delta U_f = 0.05 \text{ m/s}$ is added to the local streamwise velocity. The pipe-averaged flow velocity is $U_{avg} = 0.5 \text{ m/s}$. **b** Streamwise position fluctuation amplitude Δx as a function of ΔU_f for the particle considered in **a**.

Discussion

We would like to point out that fluid shear within the boundary layer can induce rotation in a levitated spherical particle. This rotation results in a lift force due to the Magnus effect and can also cause a deviation in the drag coefficient C_D from the standard expression given in Eq. (3). These effects become significant for large particles and in regions with high velocity gradients. However, for the micron-sized particles considered in our proposed PLV system, we estimate that these deviations are minimal. Based on the correlations reported by Ryoichi *et al.*⁶³, we calculate that both the deviation in C_D and the ratio of lift force to particle gravity should remain below a few percent for all particle sizes and flow conditions used in our calculations. To eliminate the effects of particle rotation due to flow shear, one could consider fabricating the particles to be slightly non-spherical. Non-spherical particles tend to orient in a specific direction within the magnetic trap, effectively preventing undesired rotation caused by the flow. This design strategy may help improving measurement accuracy.

We would also like to highlight that multiple particles with different diameters can be placed in the storage pit from the beginning. Additionally, by coating Teflon or other plastic beads with niobium, it is possible to produce particles with varying overall densities. This introduces an interesting dynamic: particles of the same density but different sizes will be levitated at nearly the same height but displaced to different downstream locations in the presence of LHe flow. Conversely, particles of the same size but different densities would experience similar downstream displacements but will be levitated at different heights. By introducing multiple particles and simultaneously measuring their motion, one can capture both temporal and spatial correlations of velocity fluctuations within the boundary layer. This multi-particle approach offers a unique opportunity to study turbulence structures and correlations in the thin boundary layer, providing a level of detail that is otherwise impractical to achieve. In summary, the combination of the PLV system and the distinctive properties of LHe in a cryogenic environment opens up exciting new possibilities, fully unlocking the potential of LHe in high Reynolds number turbulence research.

Methods

Magnetic field generated by the coils

Consider a single solenoid, which is a cylindrical coil of length $2L$ and radius R , tightly wound with closely packed current loops. The solenoid is centered at the origin of a cylindrical coordinate system (ρ, ϕ, z) , with its axis aligned along the z -axis.

Let I represent the current in each loop, and N denote the total number of loops. The magnetic field generated by this solenoid in three-dimensional space can be calculated using the Biot-Savart law⁶⁴. In terms of elliptic integrals^{65,66}, the magnetic field can be expressed as:

$$B_\rho = \frac{\mu_0 N I R}{\pi} [\alpha_+ P_1(k_+) - \alpha_- P_1(k_-)] \quad (5)$$

$$B_z = \frac{\mu_0 N I R}{\pi(\rho + R)} [\beta_+ P_2(k_+) - \beta_- P_2(k_-)]. \quad (6)$$

Due to axial symmetry, B_ϕ component is absent. Functions P_1 and P_2 are defined as:

$$P_1(k) = K(k) - \frac{2}{k^2} [K(k) - E(k)] \quad (7)$$

$$P_2(k) = -\frac{\gamma}{1-\gamma^2} [\Pi(1-\gamma^2, k) - K(k)] - \frac{1}{1-\gamma^2} [\gamma^2 \Pi(1-\gamma^2, k) - K(k)] \quad (8)$$

where

$$\alpha_\pm = \frac{1}{\sqrt{\xi_\pm^2 + (\rho + R)^2}} \quad \beta_\pm = \xi_\pm \alpha_\pm \quad \xi_\pm = z \pm L \quad \gamma = \frac{\rho - R}{\rho + R} \quad k_\pm^2 = \frac{4\rho R}{\xi_\pm^2 + (\rho + R)^2} \quad (9)$$

and the functions $K(k)$, $E(k)$, and $\Pi(1-\gamma^2, k)$ are the complete elliptic integrals of the first, second, and third kind:

$$\left\{ \begin{array}{l} K(k) = \int_0^{\frac{\pi}{2}} \frac{d\theta}{\sqrt{1-k^2 \sin^2 \theta}} \\ E(k) = \int_0^{\frac{\pi}{2}} \sqrt{1-k^2 \sin^2 \theta} d\theta \\ \Pi(1-\gamma^2, k) = \int_0^{\frac{\pi}{2}} \frac{d\theta}{[1-(1-\gamma^2) \sin^2 \theta] \sqrt{1-k^2 \sin^2 \theta}} \end{array} \right. \quad (10)$$

In our analysis, we calculate the magnetic field produced by each superconducting coil $\mathbf{B}_i(\mathbf{r})$ with $i = 1, 2, 3, 4$. The total magnetic field $\mathbf{B}(\mathbf{r})$ is the sum of the contributions from all individual coils $\mathbf{B}(\mathbf{r}) = \sum_{i=1}^4 \mathbf{B}_i(\mathbf{r})$.

Key parameter specifications for numerical analysis

In our study, we used MATLAB to perform several key calculations: 1) the magnetic field, $\mathbf{B}(\mathbf{r})$, generated by the coils; 2) contour plots of the volumetric potential energy $E(\mathbf{r})$ for superconducting niobium particles in the magnetic field; and 3) the motion of levitated particles under various LHe flows in the pipe. Given the axial symmetry of the coil system, we employed a computational domain of $16 \times 12 \text{ mm}^2$ in the x - y plane, with the x -axis pointing in the flow direction and the y -axis aligned along the coils' axial direction. This domain was discretized using a square grid with a spatial resolution of $10 \mu\text{m}$ in both directions. For the particle motion calculations, a time step of $50 \mu\text{s}$ was used. The chosen grid size and time step were validated by confirming that the results were independent of both parameters, ensuring convergence. The particle was assumed to be pure niobium, with a density of 8570 kg/m^3 , a critical temperature of 9.2 K , and a lower critical magnetic field of 0.15 T at 4.2 K . The LHe was modeled with a density of 145 kg/m^3 and a kinematic viscosity of $8.929 \times 10^{-9} \text{ m}^2/\text{s}$ ⁴⁹. The friction factor for LHe in high Reynolds number pipe flows has been reported in the literature^{61,62}. For instance, for a LHe pipe flow with $\text{Re} = 1.12 \times 10^6$ considered in our analysis, the friction factor is $f = 0.0124$. The particle's levitation point was determined by locating the minimum energy point within the trapping region.

References

1. Womack, K. M., Meneveau, C. & Schultz, M. P. Comprehensive shear stress analysis of turbulent boundary layer profiles. *J. Fluid Mech.* **879**, 360–389, DOI: <https://doi.org/10.1017/jfm.2019.673> (2019).
2. Johnston, J. P. & Flack, K. A. Review—Advances in three-dimensional turbulent boundary layers with emphasis on the wall-layer regions. *J. Fluids Eng.* **118**, 219–232, DOI: <https://doi.org/10.1115/1.2817367> (1996).
3. Smits, A. J., McKeon, B. J. & Marusic, I. High-Reynolds number wall turbulence. *Annu. Rev. Fluid Mech.* **43**, 353–375, DOI: <https://doi.org/10.1146/annurev-fluid-122109-160753> (2011).
4. Jiménez, J. Near-wall turbulence. *Phys. Fluids* **25**, DOI: <https://doi.org/10.1063/1.4824988> (2013).
5. White, F. M. & Majdalani, J. *Viscous fluid flow*, vol. 3 (McGraw-Hill New York, 2006).

6. Patel, A., Boersma, B. J. & Pecnik, R. The influence of near-wall density and viscosity gradients on turbulence in channel flows. *J. Fluid Mech.* **809**, 793–820, DOI: <https://doi.org/10.1017/jfm.2016.689> (2016).
7. Hultmark, M., Vallikivi, M., Bailey, S. C. C. & Smits, A. J. Turbulent pipe flow at extreme Reynolds numbers. *Phys. Rev. Lett.* **108**, 094501, DOI: <https://link.aps.org/doi/10.1103/PhysRevLett.108.094501> (2012).
8. Furuichi, N., Terao, Y., Wada, Y. & Tsuji, Y. Friction factor and mean velocity profile for pipe flow at high Reynolds numbers. *Phys. Fluids* **27**, DOI: <https://doi.org/10.1063/1.4930987> (2015).
9. Zagarola, M., Smits, A., Orszag, S. & Yakhov, V. Experiments in high Reynolds number turbulent pipe flow. In *34th Aerospace Sciences Meeting and Exhibit*, 654, DOI: <https://doi.org/10.2514/6.1996-654> (1996).
10. Österlund, J. M., Johansson, A. V., Nagib, H. M. & Hites, M. H. A note on the overlap region in turbulent boundary layers. *Phys. Fluids* **12**, 1–4, DOI: <https://doi.org/10.1063/1.870250> (2000).
11. Örlü, R. *et al.* Reynolds stress scaling in pipe flow turbulence—first results from ciclope. *Philos. Transactions Royal Soc. A: Math. Phys. Eng. Sci.* **375**, 20160187, DOI: <https://doi.org/10.1098/rsta.2016.0187> (2017).
12. Monty, J. P. *Developments in smooth wall turbulent duct flows*. Ph.D. thesis, The University of Melbourne (2005).
13. Wu, X. & Moin, P. A direct numerical simulation study on the mean velocity characteristics in turbulent pipe flow. *J. Fluid Mech.* **608**, 81–112, DOI: <https://doi.org/10.1017/S0022112008002085> (2008).
14. Lee, M. & Moser, R. D. Direct numerical simulation of turbulent channel flow up to $Re_\tau \approx 5200$. *J. fluid mechanics* **774**, 395–415, DOI: <https://doi.org/10.1017/jfm.2015.268> (2015).
15. Yamamoto, Y. & Tsuji, Y. Numerical evidence of logarithmic regions in channel flow at $Re_\tau = 8000$. *Phys. Rev. Fluids* **3**, 012602, DOI: <https://doi.org/10.1103/PhysRevFluids.3.012602> (2018).
16. Marusic, I. *et al.* Wall-bounded turbulent flows at high Reynolds numbers: recent advances and key issues. *Phys. fluids* **22**, DOI: <https://doi.org/10.1063/1.3453711> (2010).
17. McKeon, B. & Sreenivasan, K. Introduction: scaling and structure in high Reynolds number wall-bounded flows, DOI: <https://doi.org/10.1098/rsta.2006.1952> (2007).
18. Zagarola, M. V. & Smits, A. J. Mean-flow scaling of turbulent pipe flow. *J. Fluid Mech.* **373**, 33–79, DOI: <https://doi.org/10.1017/S0022112098002419> (1998).
19. Mckeon, B. J., Li, J., Jiang, W., Morrison, J. F. & Smits, A. J. Further observations on the mean velocity distribution in fully developed pipe flow. *J. Fluid Mech.* **501**, 135–147, DOI: <https://doi.org/10.1017/S0022112003007304> (2004).
20. Nagib, H. M., Chauhan, K. A. & Monkewitz, P. A. Approach to an asymptotic state for zero pressure gradient turbulent boundary layers. *Philos. Transactions Royal Soc. A: Math. Phys. Eng. Sci.* **365**, 755–770, DOI: <https://doi.org/10.1098/rsta.2006.1948> (2007).
21. Zanon, E.-S., Durst, F. & Nagib, H. Evaluating the law of the wall in two-dimensional fully developed turbulent channel flows. *Phys. fluids* **15**, 3079–3089, DOI: <https://doi.org/10.1063/1.1608010> (2003).
22. Nickels, T., Marusic, I., Hafez, S., Hutchins, N. & Chong, M. Some predictions of the attached eddy model for a high Reynolds number boundary layer. *Philos. Transactions Royal Soc. A: Math. Phys. Eng. Sci.* **365**, 807–822, DOI: <https://doi.org/10.1098/rsta.2006.1950> (2007).
23. Furuichi, N., Terao, Y., Wada, Y. & Tsuji, Y. Further experiments for mean velocity profile of pipe flow at high Reynolds number. *Phys. Fluids* **30**, DOI: <https://doi.org/10.1063/1.5017261> (2018).
24. Stainback, P. & Nagabushana, K. Review of hot-wire anemometry techniques and the range of their applicability for various flows. *Electron. J. Fluids Eng.* **1**, 4 (1993).
25. Vukoslavčević, P., Wallace, J. M. & Balint, J.-L. The velocity and vorticity vector fields of a turbulent boundary layer. Part 1. Simultaneous measurement by hot-wire anemometry. *J. Fluid Mech.* **228**, 25–51, DOI: <https://doi.org/10.1017/S0022112091002628> (1991).
26. Wilmarth, W. Pressure fluctuations beneath turbulent boundary layers. *Annu. Rev. Fluid Mech.* **7**, 13–36, DOI: <https://doi.org/10.1146/annurev.fl.07.010175.000305> (1975).
27. Bailey, S. C. *et al.* Turbulence measurements using a nanoscale thermal anemometry probe. *J. Fluid Mech.* **663**, 160–179, DOI: <https://doi.org/10.1017/S0022112010003447> (2010).
28. Javed, Y., Mansoor, M. & Shah, I. A. A review of principles of mems pressure sensing with its aerospace applications. *Sens. Rev.* **39**, 652–664, DOI: <https://doi.org/10.1108/SR-06-2018-0135> (2019).

29. Adrian, R. J. *et al.* Particle-imaging techniques for experimental fluid mechanics. *Annu. Rev. Fluid Mech.* **23**, 261–304, DOI: <https://doi.org/10.1146/ANNUREV.FL.23.010191.001401> (1991).
30. Van Oudheusden, B. PIV-based pressure measurement. *Meas. Sci. Technol.* **24**, 032001, DOI: <https://doi.org/10.1088/0957-0233/24/3/032001> (2013).
31. de Silva, C. M., C. M. *et al.* High spatial range velocity measurements in a high Reynolds number turbulent boundary layer. *Phys. fluids* **26**, DOI: <https://doi.org/10.1063/1.4866458> (2014).
32. Scarano, F. Tomographic PIV: principles and practice. *Meas. Sci. Technol.* **24**, 012001, DOI: <https://doi.org/10.1088/0957-0233/24/1/012001> (2012).
33. Adamczyk, A. & Rimai, L. 2-Dimensional particle tracking velocimetry (PTV): technique and image processing algorithms. *Exp. fluids* **6**, 373–380, DOI: <https://doi.org/10.1007/BF00196482> (1988).
34. Dabiri, D. & Pecora, C. *Particle tracking velocimetry* (IOP Publishing, 2019).
35. Mastracci, B. & Guo, W. Exploration of thermal counterflow in He II using particle tracking velocimetry. *Phys. Rev. Fluids* **3**, 063304, DOI: <https://doi.org/10.1103/PhysRevFluids.3.063304> (2018).
36. Mastracci, B., Bao, S., Guo, W. & Vinen, W. F. Particle tracking velocimetry applied to thermal counterflow in superfluid ^4He : Motion of the normal fluid at small heat fluxes. *Phys. Rev. Fluids* **4**, 083305, DOI: <https://doi.org/10.1103/PhysRevFluids.4.083305> (2019).
37. Tang, Y., Bao, S., Kanai, T. & Guo, W. Statistical properties of homogeneous and isotropic turbulence in He II measured via particle tracking velocimetry. *Phys. Rev. Fluids* **5**, 084602, DOI: <https://doi.org/10.1103/PhysRevFluids.5.084602> (2020).
38. Tang, Y. *et al.* Imaging quantized vortex rings in superfluid helium to evaluate quantum dissipation. *Nat. Commun.* **14**, 2941, DOI: <https://doi.org/10.1038/s41467-023-38787-w> (2023).
39. Lavoie, P., Avallone, G., De Gregorio, F., Romano, G. P. & Antonia, R. Spatial resolution of PIV for the measurement of turbulence. *Exp. Fluids* **43**, 39–51, DOI: <https://doi.org/10.1007/s00348-007-0319-x> (2007).
40. Hoyer, K. *et al.* 3D scanning particle tracking velocimetry. *Exp. Fluids* **39**, 923–934, DOI: <https://doi.org/10.1007/s00348-005-0031-7> (2005).
41. Li, F., Zhang, H. & Bai, B. A review of molecular tagging measurement technique. *Measurement* **171**, 108790, DOI: <https://doi.org/10.1016/j.measurement.2020.108790> (2021).
42. Miles, R., Lempert, W. & Zhang, B. Turbulent structure measurements by relief flow tagging. *Fluid Dyn. Res.* **8**, 9, DOI: [10.1016/0169-5983\(91\)90027-G](https://doi.org/10.1016/0169-5983(91)90027-G) (1991).
43. Michael, J. B., Edwards, M. R., Dogariu, A. & Miles, R. B. Femtosecond laser electronic excitation tagging for quantitative velocity imaging in air. *Appl. optics* **50**, 5158–5162, DOI: <https://doi.org/10.1364/AO.50.005158> (2011).
44. Hsu, A. G., Srinivasan, R., Bowersox, R. D. & North, S. W. Two-component molecular tagging velocimetry utilizing NO fluorescence lifetime and NO₂ photodissociation techniques in an underexpanded jet flowfield. *Appl. Opt.* **48**, 4414–4423, DOI: <https://doi.org/10.1364/AO.48.004414> (2009).
45. Varga, E., Gao, J., Guo, W. & Skrbek, L. Intermittency enhancement in quantum turbulence in superfluid ^4He . *Phys. Rev. Fluids* **3**, 094601, DOI: <https://doi.org/10.1103/PhysRevFluids.3.094601> (2018).
46. Gao, J. *et al.* Producing and imaging a thin line of He₂^{*} molecular tracers in helium-4. *Rev. Sci. Instruments* **86**, 093904, DOI: <https://doi.org/10.1063/1.4930147> (2015).
47. Marakov, A. *et al.* Visualization of the normal-fluid turbulence in counterflowing superfluid ^4He . *Phys. Rev. B* **91**, 094503, DOI: <https://doi.org/10.1103/PhysRevB.91.094503> (2015).
48. Guo, W. Molecular tagging velocimetry in superfluid helium-4: Progress, issues, and future development. *J. Low Temp. Phys.* **196**, 60–72, DOI: <https://doi.org/10.1007/s10909-018-2102-1> (2019).
49. Donnelly, R. J. & Barenghi, C. F. The observed properties of liquid helium at the saturated vapor pressure. *J. Phys. Chem. Ref. Data* **27**, 1217–1274 (1998).
50. Donnelly, R. J. *High Reynolds Number Flows Using Liquid and Gaseous Helium: Discussion of Liquid and Gaseous Helium as Test Fluids Including papers from The Seventh Oregon Conference on Low Temperature Physics, University of Oregon, October 23–25, 1989* (Springer Science & Business Media, 2012).
51. Skrbek, L., Niemela, J. & Donnelly, R. Turbulent flows at cryogenic temperatures: a new frontier. *J. Physics: Condens. Matter* **11**, 7761, DOI: <https://doi.org/10.1088/0953-8984/11/40/308> (1999).

52. Donnelly, R. J. & Streenivasan, K. R. *Flow at Ultra-High Reynolds and Rayleigh Numbers: A Status Report* (Springer Science & Business Media, 2012).
53. Sanavandi, H. *et al.* A cryogenic-helium pipe flow facility with unique double-line molecular tagging velocimetry capability. *Rev. Sci. Instruments* **91**, DOI: <https://doi.org/10.1063/5.0008117> (2020).
54. Ikushima, A. & Mizusaki, T. Superconductivity in niobium and niobium-tantalum alloys. *J. Phys. Chem. Solids* **30**, 873–879, DOI: [https://doi.org/10.1016/0022-3697\(69\)90283-2](https://doi.org/10.1016/0022-3697(69)90283-2) (1969).
55. Yamato, M. & Kimura, T. Magnetic processing of diamagnetic materials. *Polymers* **12**, 1491, DOI: <https://doi.org/10.3390/polym12071491> (2020).
56. Finnemore, D., Stromberg, T. & Swenson, C. Superconducting properties of high-purity niobium. *Phys. Rev.* **149**, 231, DOI: <https://doi.org/10.1103/PhysRev.149.231> (1966).
57. Arrayás, M., Trueba, J. L., Uriarte, C. & Zmeev, D. E. Design of a system for controlling a levitating sphere in superfluid ^3He at extremely low temperatures. *Sci. Reports* **11**, 20069, DOI: <https://doi.org/10.1038/s41598-021-99316-7> (2021).
58. Hemmati, A., Fuzier, S., Bosque, E. & Van Sciver, S. Drag measurement on an oscillating sphere in Helium II. *J. Low Temp. Phys.* **156**, 71–83, DOI: <https://doi.org/10.1007/s10909-009-9890-2> (2009).
59. Melling, A. Tracer particles and seeding for particle image velocimetry. *Meas. Sci. Technol.* **8**, 1406, DOI: <https://doi.org/10.1088/0957-0233/8/12/005> (1997).
60. Sanavandi, H. *Liquid Helium Turbulent Pipe Flow and Magnetic Levitation Research*. Ph.D. thesis, The Florida State University (2022).
61. Swanson, C. J., Donnelly, R. J. & Ihas, G. G. Turbulent pipe flow of He I and He II. *Phys. B: Condens. Matter* **284**, 77–78, DOI: [https://doi.org/10.1016/S0921-4526\(99\)02042-6](https://doi.org/10.1016/S0921-4526(99)02042-6) (2000).
62. Walstrom, P., Weisend II, J., Maddocks, J. & Van Sciver, S. Turbulent flow pressure drop in various He II transfer system components. *Cryogenics* **28**, 101–109, DOI: [https://doi.org/10.1016/0011-2275\(88\)90054-9](https://doi.org/10.1016/0011-2275(88)90054-9) (1988).
63. Kurose, R. & Komori, S. Drag and lift forces on a rotating sphere in a linear shear flow. *J. Fluid Mech.* **384**, 183–206, DOI: <https://doi.org/10.1017/S0022112099004164> (1999).
64. Jackson, J. A curious and useful theorem in two-dimensional electrostatics. *Am. J. Phys.* **67**, 107–115, DOI: <https://doi.org/10.1119/1.19203> (1999).
65. Caciagli, A., Baars, R. J., Philipse, A. P. & Kuipers, B. W. Exact expression for the magnetic field of a finite cylinder with arbitrary uniform magnetization. *J. Magn. Magn. Mater.* **456**, 423–432, DOI: <https://doi.org/10.1016/j.jmmm.2018.02.003> (2018).
66. Derby, N. & Olbert, S. Cylindrical magnets and ideal solenoids. *Am. J. Phys.* **78**, 229–235, DOI: <https://doi.org/10.1119/1.3256157> (2010).

Acknowledgements

Y.Q. and W.G. acknowledge support from the Gordon and Betty Moore Foundation through Grant DOI 10.37807/gbmf11567. This work was conducted at the National High Magnetic Field Laboratory at Florida State University, supported by the National Science Foundation Cooperative Agreement No. DMR-2128556 and the state of Florida. The authors also wish to thank Lauren Roche for her assistance in the design of the superconducting coils.

Author contributions statement

W.G. designed the research. Y.Q. designed the coil configuration and conducted the numerical simulations. Y.Q. and W.G. analyzed the results and collaboratively wrote and reviewed the manuscript.

Data availability statement

The datasets used and/or analysed during the current study available from the corresponding author on reasonable request.

Additional information

Competing interests: The authors declare no competing interests.